



Relationships between Thin clouds, Opaque Clouds, and the Tropical Easterly Jet over the Indian Region observed with Aeolus Spaceborne Doppler Wind Lidar

Zacharie Titus¹, Marine Bonazzola¹, Hélène Chepfer¹, Artem Feofilov¹, and Marie-Laure Roussel¹

Laboratoire de Météorologie Dynamique / IPSL, Sorbonne Université, Institut Polytechnique de Paris, CNRS, Palaiseau, France

Correspondence: Zacharie Titus (zacharie.titus@lmd.ipsl.fr)

Abstract.

Direct wind observations used to be rare over the Arabian Sea and the Bay of Bengal. Since the launch of ESA's Aeolus Doppler Wind Lidar, profiles of horizontal wind are acquired every day and are perfectly co-located with profiles of thin and opaque clouds. In this study, we show that from June to October 2020, during the South-Asian Summer Monsoon (SASM), high altitude clouds formed over the Bay of Bengal by deep convection in the afternoon are advected westward towards the Arabian Sea in the morning by the fast winds of the Tropical Easterly Jet (TEJ). Consequently, the thin high cloud cover over the Arabian Sea is 14 % at 06 LT on days where westward winds are faster than 23.6 ms⁻¹ between 14 and 17 km of altitude, more than twice as much than on days where westward winds are slower than 23.6 ms⁻¹ (6 %). While the TEJ is primarily driven by the thermal contrast between warm land and cooler Indian Ocean, we observe that the diverging-rotating outflow around deep convective (opaque) clouds can strengthen or weaken the TEJ over the Arabian Sea with respect to the thermal wind, explaining a 3 ms⁻¹ amplitude variation during the SASM. These results suggest that the cirrus cloud cover over the Arabian Sea may decrease in the next decades, as the TEJ and the convection over the Eastern Indian Ocean are expected to decrease in intensity.





15 1 Introduction

Tropical deep convection leads to the formation of high altitude clouds that can reach up to 17 km of altitude around India (Mehta, 2024). At its top, the cloud spreads out horizontally away from the convective core to form an anvil cloud (Betts, 1973; Ackerman et al., 1988). The edge of the anvil cloud, optically thinner, can be detrained further away from the core by the local dynamics. Detrained cirrus represent about half of cirrus occurrences (Massie et al., 2002; Luo and Rossow, 2004) while the other half of cirrus are formed "in-situ" (i.e. they do not directly originate from deep convection). Cirrus can be advected over distances larger than 1000 km (Luo and Rossow, 2004). They live for a few hours up to a few days until they are dissipated by solar warming (Chepfer et al., 2019), gravity waves interactions (Corcos et al., 2023) or sedimentation of ice crystals (Stubenrauch et al., 2019; Jensen et al., 2025). The balance between the size of the convective core and the anvil area in a deep convective cloud is subject to change in a warming world (Höjgård-Olsen et al., 2022; McKim et al., 2024). This change should be evaluated as a variation in the ratio between opaque and thin high cloud covers might affect the radiative effect of these clouds (Hartmann and Berry, 2017; Gasparini et al., 2021).

In this study, we focus on the Indian region during the South Asian Summer Monsoon (SASM), characterized by a strong convection over the Indian continent and the Bay of Bengal, and at the same time by a fast westward wind in the upper troposphere reaching more than 30 ms⁻¹, the Tropical Easterly Jet (TEJ). This region is the theatre of a subtle interplay between temperature, deep convection, the TEJ and the cirrus cover: the temperature contrast controls the TEJ speed via the thermal wind balance, and the TEJ speed is also controlled by, or controls, the occurrence and locations of deep convection. Deep convection acts as a source of water vapour in the upper troposphere which forms cirrus clouds that may extend over large distances depending on the speed of the TEJ and temperature conditions. In turn, the cirrus cloud cover may affect temperatures of the upper troposphere by its radiative effect.

Das et al. (2011) have noticed that during the period where both deep convection and TEJ are active, a larger cirrus cover is observed over the Indian region. They concluded on the role of advection of humidity by the TEJ through the cold temperatures of the upper troposphere in the formation of cirrus clouds over this region. The TEJ is mainly due to a large thermal contrast in the upper troposphere between the heated, elevated Tibetan plateau region and the cooler Indian Ocean region (Koteswaram, 1958). Chen (1982) suggested that in addition to this mechanism, the TEJ is energetically maintained by the release of available potential energy by the tropical divergent circulation associated with both the north-south (Hadley) and the east-west (Walker) circulations. He showed that the kinetic energy of the easterly jet is generated on the upstream side where an upward branch of the East-West Walker circulation is located (Chen, 1982). The interannual variation of the TEJ may thus be explained by changes of the tropical divergent circulations (Chen and van Loon, 1987). Pattanaik and Satyan (2000) indeed showed a strong interannual variability of the TEJ during El Niño/La Niña years, with an intensity of the TEJ positively correlated with the summer monsoon rainfall over India. In a warming climate, Huang et al. (2020) also showed that the CMIP-6 projected El Niño-like warming pattern over the tropical Pacific may play a critical role in the future weakening of the TEJ, via suppressing



80



rainfall over the tropical eastern Indian Ocean and maintaining an upper-level convergence, leading to slower easterly winds in the upper troposphere over most of the Indian Ocean. Rao et al. (2004) proved with NCEP/NCAR reanalyses and radiosonde data the existence of a strong correlation between the speed of the TEJ and the number of tropical cyclones over the Bay of Bengal for a period of more than 40 years. They interpreted this correlation by the higher growth rates of monsoon depressions due to strong easterly wind shears. More recently, Ye et al. (2023) observed that the location of the core of the TEJ exhibits a large interannual longitudinal variability around India, and particularly in July. Liu et al. (2024) further showed that this variability had two modes and that the core of the TEJ is whether located over the Arabian Sea or on the South-West of India. They demonstrated that a deep convection dipole located over the East Arabian Sea and the Bay of Bengal is the main driver of this interannual variability of the TEJ core location.

Although the variations of the TEJ at the synoptic and intraseasonal scales received less attention, Sathiyamoorthy et al. (2007) noted a concomitant shifting of the locations of deep convection, low level monsoon flow and TEJ during the different phases of the SASM, suggesting that they all may be related. Some authors studied the link between the TEJ and Sahel rainfall at these time scales. Nicholson (2009) suggested that there is a causal relationship between the TEJ and Sahel rainfall, with a faster TEJ enhancing rainfall by strengthening the upper-level divergence. Diongue et al. (2002) showed that the diverging-rotating outflow at the top of Deep Convective Systems (DCS) over West Africa induces a westward wind anomaly at the South-West of the DCS. The westward wind anomaly is maximum one or two days after the growth of the DCS (Lemburg et al., 2019). This indicates that deep convection anomalies are more likely to drive changes in the regional TEJ than vice versa.

The aim of this study is thus to investigate the relationships between thin clouds (cirrus), opaque clouds (mostly convective) and the TEJ over the Indian region during the SASM. This is particularly important as in a warming climate, a weakening of the TEJ is expected (Rao et al., 2004; Huang et al., 2020), as well as a decrease in the convection intensity over the Bay of Bengal (Rao et al., 2004). These changes are likely to impact the cirrus cloud cover over the Indian region in the future.

We make use of an Aeolus spaceborne Doppler Wind LIDAR dataset (Titus et al., 2025), which displays perfectly co-located observed profiles of clouds and profiles of horizontal winds. This dataset is particularly well adapted to our study. First, Aeolus observations are available at 06 and 18 LT, and are thus perfectly adequate to document convective clouds that develop in the late afternoon (Chepfer et al., 2019). Second, observations occurring 12 hours later are shifted westward by 1150 km, and thus offer the opportunity to observe the cirrus that are potentially detrained from convective sources by the westward TEJ. Third, the TEJ is almost purely zonal (Mohan and Rao, 2016; Iqbal et al., 2017) and is thus well observed by Aeolus, as the Aeolus Line-of-Sight (LOS) at those latitudes is also almost zonal.

The paper is structured as follows. We first shortly describe our Aeolus dataset, and the method we use to distinguish opaque clouds from thin clouds (Sect. 2). We characterize the annual variation and the diurnal contrast of winds and clouds over the Indian region (Sect. 3). We then quantify how the zonal wind affects the thin cloud cover over the Arabian Sea, and we attempt





to disentangle this effect from the respective roles of temperature and convective intensity variations (Sect. 4). Furthermore, we evaluate how different deep convection patterns above the Indian region weaken or strengthen the zonal wind through divergence and vorticity of the convective outflow (Sect. 5). We finally conclude this paper in Section 6.





2 Dataset and Method

The Aeolus satellite carries the Atmospheric LAser Doppler Instrument (ALADIN), a 355 nm spaceborne Doppler Wind Lidar with High Spectral Resolution capabilities (Stoffelen et al., 2005; Reitebuch, 2012). Aeolus is primarily designed to retrieve profiles of horizontal winds, but can also retrieve profiles of clouds (Feofilov et al., 2022; Donovan et al., 2024; Titus et al., 2025). In this study, we make use of a global wind and cloud profiles dataset observed with Aeolus (Titus et al., 2025).

2.1 Clouds

105

115

The clouds are detected at a spatial resolution of 3 km along the orbit track horizontally and 480 m vertically. Each single profile contains 40 vertical bins, and each 3 km \times 480 m bin is either classified as "clear", "cloudy" or "fully attenuated". This last category corresponds to a bin where the laser is fully attenuated because the atmosphere above the bin has an optical thickness larger than typically 3 to 5. More details are given in Sect. 2.1 of Titus et al. (2025).

We use this bin classification to discriminate between single profiles containing optically thin clouds $(0.03 < \tau < 3 \text{ to } 5)$ such as in-situ or detrained cirrus clouds, from single profiles containing optically opaque clouds $(\tau > 3 \text{ to } 5)$, such as convective clouds or the thickest part of anvil clouds, closer to the convective core (Fig. 1). To do so, in each single profile containing at least one "cloudy" bin, we evaluate if all the bins between the ground and 1 km below the lowermost cloudy bin are fully attenuated. If this is the case, then the entire single profile is flagged as "opaque" (see profiles #4 and #5, Fig. 1), otherwise, the entire single profile is flagged as "thin" (see profiles #2 and #3, Fig. 1). Single profiles which contain no cloudy layer between the ground and 18 km of altitude are simply flagged as "clear" (see profile #1, Fig. 1)

Then, we consider all the single profiles falling within 2° latitude \times 2° longitude boxes to build the gridded opaque cloud fraction profiles (CFopaque) and gridded thin cloud fraction profiles (CFthin) between the ground and 18 km of altitude. Those are three-dimensional quantities (2° longitude \times 2° latitude \times 480 m vertically), representing the number of 3 km \times 480 m cloudy bins at a given altitude level among "thin" profiles (resp. among "opaque" profiles) divided by the number of bins which are not "fully attenuated" at the same altitude level within the considered 2° longitude \times 2° latitude grid box.

We further define diagnostics at high altitude, near the TEJ, between 14 and 17 km: the opaque cloud fraction profiles at high altitude (HCFopaque), the thin cloud fraction profiles at high altitude (HCFthin), which retain the values of CFopaque (resp. CFthin) but only between 14 and 17 km of altitude instead of the entire troposphere.

In addition to the previous vertically resolved profiles, we define the thin (resp. opaque) high cloud covers HCCthin (resp. HCCopaque) which are two-dimensional (2° longitude \times 2° latitude) quantities. They represent the number of thin profiles (resp. opaque profiles) containing at least one 3 km \times 480 m cloudy bin between 14 and 17 km of altitude, divided by the total number of profiles within the considered 2° longitude \times 2° latitude grid box.





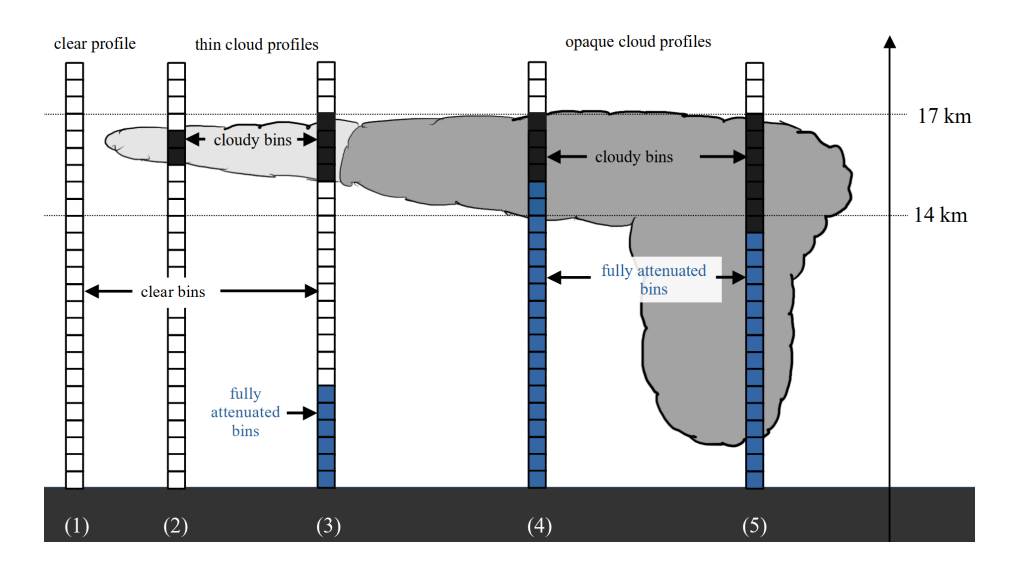


Figure 1. Schematic of the different types of profiles (clear, thin cloud and opaque cloud profiles) observed with Aeolus.

120 2.2 Winds

125

130

Hereafter, we use Aeolus profiles of horizontal wind speed, noted u_{allsky} in Titus et al. (2025). Within a single profile, the value of the horizontal wind speed u_{allsky} is given for each 480 m thick bin beside the cloud/clear flags (Sect. 2.1). We use the notation u_{allsky} for the wind (instead of the notation v_{HLOS} commonly used in the Aeolus literature) because the wind is observed both within clear and cloudy bins (but not within fully attenuated bins). We note positive (resp. negative) u_{allsky} values corresponding to eastward (resp. westward) winds.

As the laser is pointed 35 deg. off-nadir and perpendicular to the satellite track, away from the Sun, the Aeolus measurement is not the actual horizontal wind, but the horizontal projection of the wind retrieved along the Line-of-Sight (LOS) of Aeolus. However, the LOS being almost zonal at the latitudes considered in this paper (the angle between the LOS and the West-East direction is comprised between 8 and 10 deg.), Aeolus essentially retrieves the zonal component of the wind: the relative difference between the zonal component of the wind and the wind projection along the LOS is about 1 %. The restriction to the zonal component of the wind does not represent a limitation of our study, as the TEJ is also almost purely zonal (Iqbal et al., 2017).



135

140

145



3 Evolution of wind and clouds over the Indian Region

3.1 Annual variations

The Indian Region (defined as 12°N - 24°N and 53°E - 98°E) is under the influence of the Sub-Tropical Jet (STJ) from January to May, with eastward winds exceeding 30 ms⁻¹ between 10 and 14 km of altitude (Fig. 2a). During the same period, both *CFthin* and *CFopaque* observed by Aeolus, remain below 10 % (Fig. 2b, 2c). As the South-Asian Summer Monsoon (SASM) onsets in late May, a reversal of the wind (from eastward to westward) is observed. This so-called Tropical Easterly Jet (TEJ) is embedded within an anticyclonic circulation over the Indian region (Koteswaram, 1958; Krishnamurti et al., 1973), and is essentially induced by a thermal gradient between the warm upper troposphere over the Tibetan plateau and the cooler upper troposphere over the Indian Ocean (Koteswaram, 1958). From mid-June to August, the TEJ is maintained and exceeds 30 ms⁻¹ between 14 and 17 km of altitude, before decaying in September (Fig. 2a). The wind still remains westward until late October. During the active phase of SASM (late May - October), *CFopaque* larger than 30 % and *CFthin* larger than 15 % are frequently observed over the Indian region between 14 and 17 km of altitude (Fig. 2b, 2c). Note that over the entire Indian region, profiles of *CFopaque* and *CFthin*, estimated from the same orbits of Aeolus are well correlated. When SASM decays in late October, the Inter Tropical Convergence Zone (ITCZ) migrates southward and winds reverse again (from westward to eastward) as the STJ becomes the dominant zonal circulation (Fig. 2a). After the break of SASM, *CFopaque* and *CFthin* fall below 5 % between 14 and 17 km of altitude (Fig. 2b, 2c).



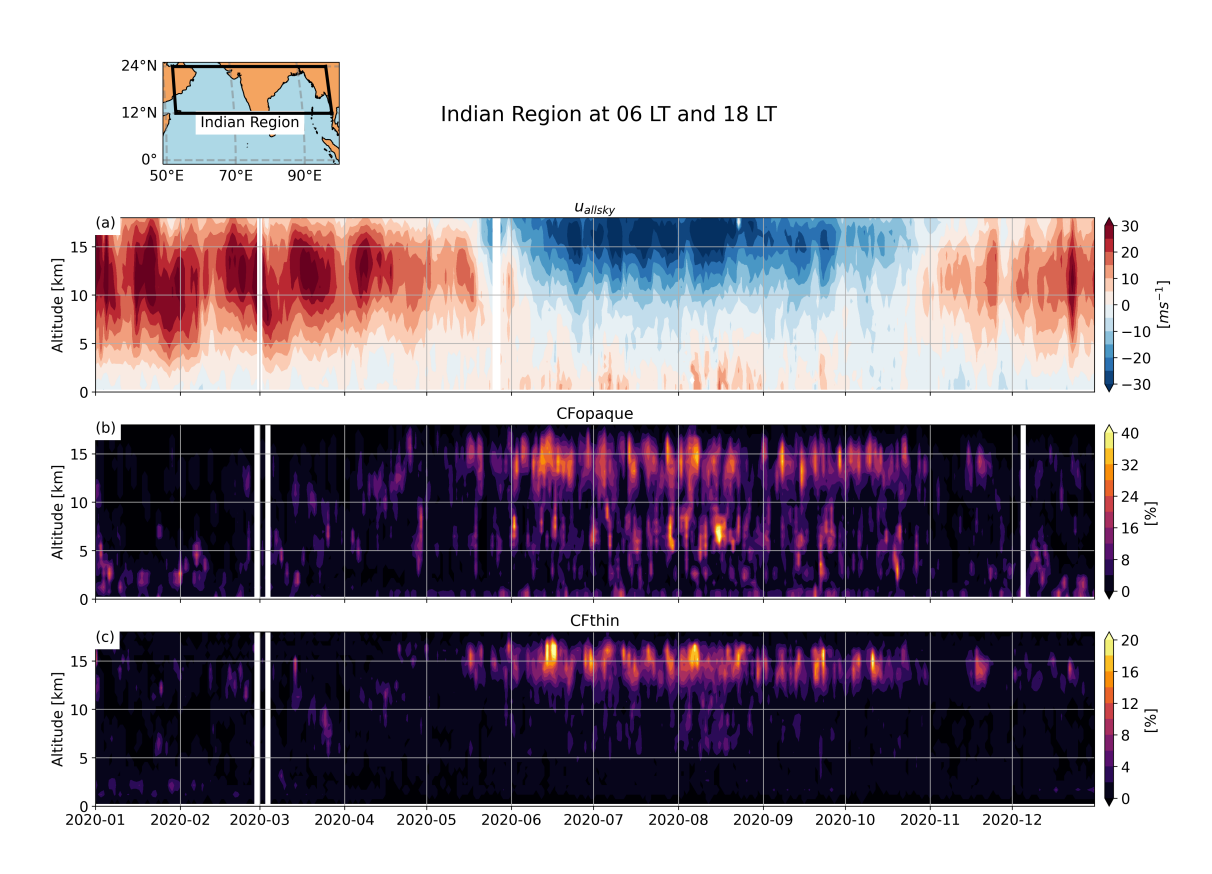


Figure 2. (a) Time series of profiles of u_{allsky} observed from Aeolus in 2020. Note that negative u_{allsky} values denote a westward wind while positive u_{allsky} values denote an eastward wind. (b) Opaque cloud fraction profiles CFopaque and (c) thin cloud fraction profiles CFthin observed from Aeolus in 2020. For readability purposes, colorbar ranges are different for opaque cloud fraction profiles (0-40 %) and thin cloud fraction profiles (0-20 %).



150



3.2 Diurnal contrast

Figures 3a and 3b show HCCopaque observed during the active phase of SASM (June-October) at 18 LT and 06 LT respectively. HCCopaque is in general larger at 18 LT than at 06 LT. At 18 LT, the maxima of HCCopaque between 14 and 17 km of altitude are located over the North-East of India (20°N, 80°E) and the South-West of the Bay of Bengal (12°N, 85°E), and reach 30 % (Fig. 3a). At 18 LT, the HCCopaque maximum over the North-East of India is expected as continental deep convection peaks in the late afternoon, around 18 LT, before decaying during the night (Mapes and Houze Jr, 1993; Noel et al., 2018; Chepfer et al., 2019) to about 15 % at 06 LT (Fig. 3b). At the opposite, over the North-East of the Bay of Bengal (15°N, 90°E) that is more under maritime influence, HCCopaque is slightly below 20 %, at 18 LT (Fig. 3a) and increases to 25 %, at 06 LT (Fig. 3b). The diurnal contrast of HCCopaque observed with Aeolus during the 2020 SASM over the Bay of Bengal is in good agreement with the diurnal cycle of cold, deep convective high cloud cover observed with passive imagery (Zuidema, 2003; Feofilov and Stubenrauch, 2019), in spite of the large inter-annual variations of the cloud patterns and precipitation over the Indian region (Krishnamurthy and Shukla, 2000) and the specificity of the 2020 SASM (Kripalani et al., 2022). The Arabian Sea received less attention than the Bay of Bengal when it comes to deep convection. We observe a diurnal contrast of HCCopaque, with a HCCopaque about 5 % larger at 18 LT than at 06 LT over the entire Arabian Sea (Fig. 3c). This difference increases to about 12 % on the South-East of the Arabian Sea (10°N, 65°E, Fig. 3c), most likely due to a large diurnal cycle of sea surface temperature (SST) (Chen and Houze Jr, 1997). Indeed, the SST at this location can warm up by around 2 K during a single day between 04 LT and 16 LT between the months of June to September, as observed by Shenoi et al. (2009). Over the North-East Arabian Sea (20°N, 65°E), HCCopaque is the same (Fig. 3c) (about 15 %), at both 18 LT (Fig. 3a) and 06 LT (Fig. 3b).

HCCthin also exhibits a diurnal contrast between 18 LT and 06 LT (Fig. 3f), although not as pronounced as HCCopaque. At 18 LT, the HCCthin reaches values of about 20 % over continental India (Fig. 3d) and similar values above the entire Bay of Bengal. At 06 LT, HCCthin remains at about 20 % over continental India (Fig. 3e), as observed by Ali et al. (2022). One of the main reasons why the HCCthin diurnal contrast is much weaker than that of HCCopaque is that part of the opaque clouds resulting from deep convection at 18 LT are converted to thin clouds during the night. Over the Arabian Sea, characterized by a weaker deep convection at 18 LT, the HCCthin is only 2 to 4 % larger at 18 LT than at 06 LT. The ratio between HCCthin and HCCopaque both measured over the Arabian Sea is much larger at 06 LT than at 18 LT, which indicates that a non negligible part of thin clouds observed at 06 LT might have a non-local convective origin. We also observe that the zonal gradient of HCCthin over the Arabian Sea at 18 LT (8 % at 50°E to 14 % at 70°E, Fig. 3d) is less pronounced than the zonal gradient of HCCopaque at 18 LT (6 % at 50°E to 20 % at 70°E, Fig. 3a). This longitudinal extension of thin clouds was also reported by Yang et al. (2010) and Das et al. (2011).

While Das et al. (2011) observed an increase of the thin cloud cover with the wind over the entire Indian region, Fig. 3 suggests that this relationship might be even stronger when focusing on the Arabian Sea at 06 LT. Indeed, the winds are





strongest in this region at this local time (Fig. 3g, 3h), the ratio between *HCCthin* and *HCCopaque* seems to be maximal there, and convection, which is the main source of water vapour at these altitudes, is located upstream, over the Bay of Bengal and North-East India at 18 LT (Fig. 3a). In the following, we will thus focus our analysis on high thin clouds over the Arabian Sea at 06 LT.

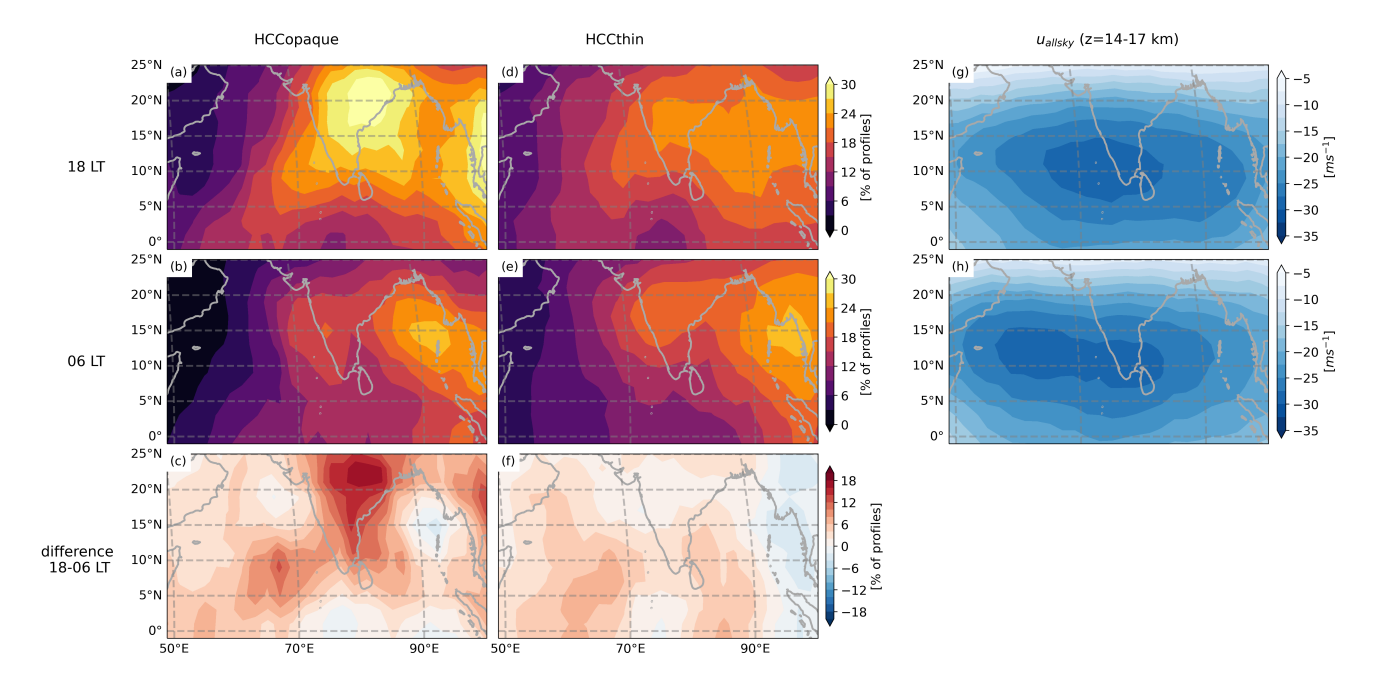


Figure 3. Map of average opaque high cloud cover HCC opaque between 14-17 km, from June to October 2020 at (a) 18 LT and (b) 06 LT (c) is the difference of (a)-(b). Map of average thin high cloud cover HCC thin between 14-17 km, from June to October 2020 at (d) 18 LT and (e) 06 LT. (f) is the difference of (d)-(e). Map of u_{allsky} averaged between 14-17 km, from June to October 2020 at 18 LT (g) and 06 LT (h).





195

200

4 Thin high clouds over the Arabian Sea are advected by the Tropical Easterly Jet

In this section, we combine orbits of Aeolus over the Bay of Bengal at 18 LT and over the Arabian Sea at 06 LT as shown in Fig. 4, to compare the cloudiness over each region and assess the role of the zonal wind in transporting clouds from the Bay of Bengal and the Indian continent to the Arabian Sea.

We define two domains around India, based on our high cloud cover observations of Fig. 3. One domain encompasses the Arabian Sea and the other encompasses the Bay of Bengal and a large part of the India. This analysis benefits from Aeolus sun-synchronous orbit properties. Figure 4 details an entire 7-day cycle of Aeolus orbits from 8 January 2020 to 14 January 2020. On 8 January 2020, Aeolus crosses the middle of Arabian Sea domain at 06 LT, between 65°E at 24°N and 63°E at 12°N (dark blue orbit, Fig. 4). On the same day, 12 hours later, Aeolus ascending orbit overflies the Bay of Bengal domain at 18 LT on the very East, between 98°E at 12°N and 96°E at 24°N (dark blue orbit, Fig. 4). On 9 January 2020, the orbits crossing each domain are shifted by about 300 km westward compared to the previous day orbits (lighter blue orbit, Fig. 4). After 7 days, both domains are fully paved, and Aeolus follows exactly the same orbits with a 7-day periodicity. For example, Aeolus overflies the descending and ascending dark blue orbits (Fig. 4) again on 15 January 2020 at 06 and 18 LT, respectively.

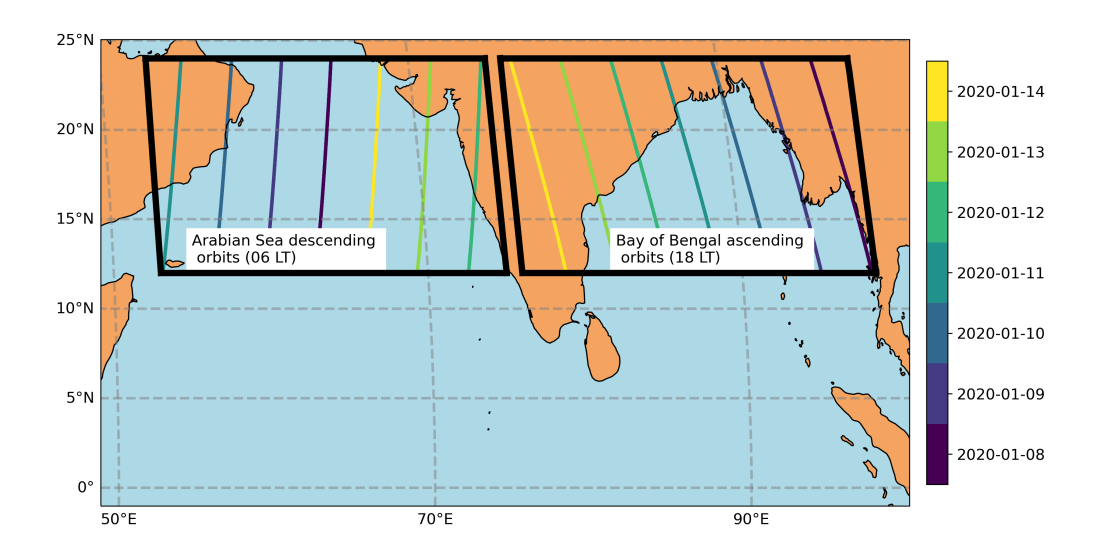


Figure 4. Aeolus descending orbits at 06 LT over the Arabian Sea (12°N - 24°N and 53°E - 75°E) and ascending orbits over the Bay of Bengal (10°N - 24°N and 76°E - 98°E) at 18 LT during a 7-day period between 8 and 14 January 2020. Each colour indicates the day of the orbit.



210

215



4.1 Relationship between thin high cloud cover and the wind over the Arabian Sea

Figure 5 shows the time series of u_{allsky} averaged between 14 and 17 km of altitude over the Arabian Sea (AS) at 06 LT, noted $\overline{u_{allsky}(AS,\ 06\ LT)}$. The bar denotes an average over all altitudes between 14 and 17 km. The median value of $\overline{u_{allsky}(AS,\ 06\ LT)}$ is -23.6 ms⁻¹ between June and October. On the days where $\overline{u_{allsky}(AS,\ 06\ LT)}$ is faster than its median value, noted "fast" wind days, the average wind speed is -29.9 \pm 4.1 ms⁻¹. In contrast, on the days where $\overline{u_{allsky}(AS,\ 06\ LT)}$ is slower than its median value, noted "slow" wind days, the average wind speed is -13.8 \pm 7.7 ms⁻¹.

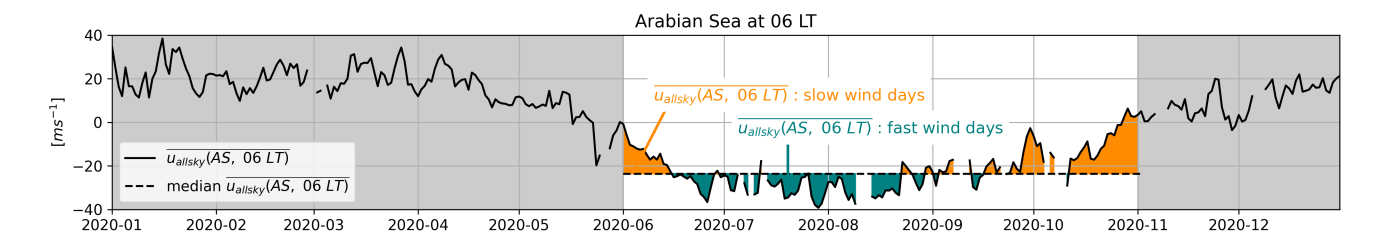


Figure 5. Time series of $\overline{u_{allsky}(AS,\ 06\ LT)}$ (solid black line), u_{allsky} is averaged each day over the Arabian Sea and averaged between 14 and 17 km of altitude at 06 LT. The dashed black line represents the median value of $\overline{u_{allsky}(AS,\ 06\ LT)}$ from June to October 2020, $-23.6\ \mathrm{ms}^{-1}$.

We select days where $\overline{u_{allsky}(AS, 06\ LT)}$ is faster (or slower) than its median value, and build the composite maps of the high thin cloud cover observed at the same time (Fig. 6). During fast wind days at 06 LT, HCCthin reaches 25 % near the West coast of India (18°N, 70°E, Fig. 6a) and 14 % on average over the Arabian Sea. On the other hand, on slow wind days, HCCthin is within the range of 2 - 15 %, and on average 6 % over the Arabian Sea at 06 LT (Fig. 6b). The HCCthin differences between fast and slow wind days (Fig. 6c) are largest over the Arabian Sea in the North of 20°N, where they reach 12 %. The dependence of HCCthin on the wind speed, detailed by Das et al. (2011), is thus also observed in our study. We note that when spatially averaged over the Arabian Sea, HCCthin increases by 8 % when the wind speed over the Arabian Sea doubles (from -13.8 ms⁻¹ to -29.9 ms⁻¹). In comparison, Das et al. (2011) reported a relative increase of HCCthin of about 20 % at 150 hPa close to the core of the TEJ when the wind speed is doubled, and no increase at 70 hPa.





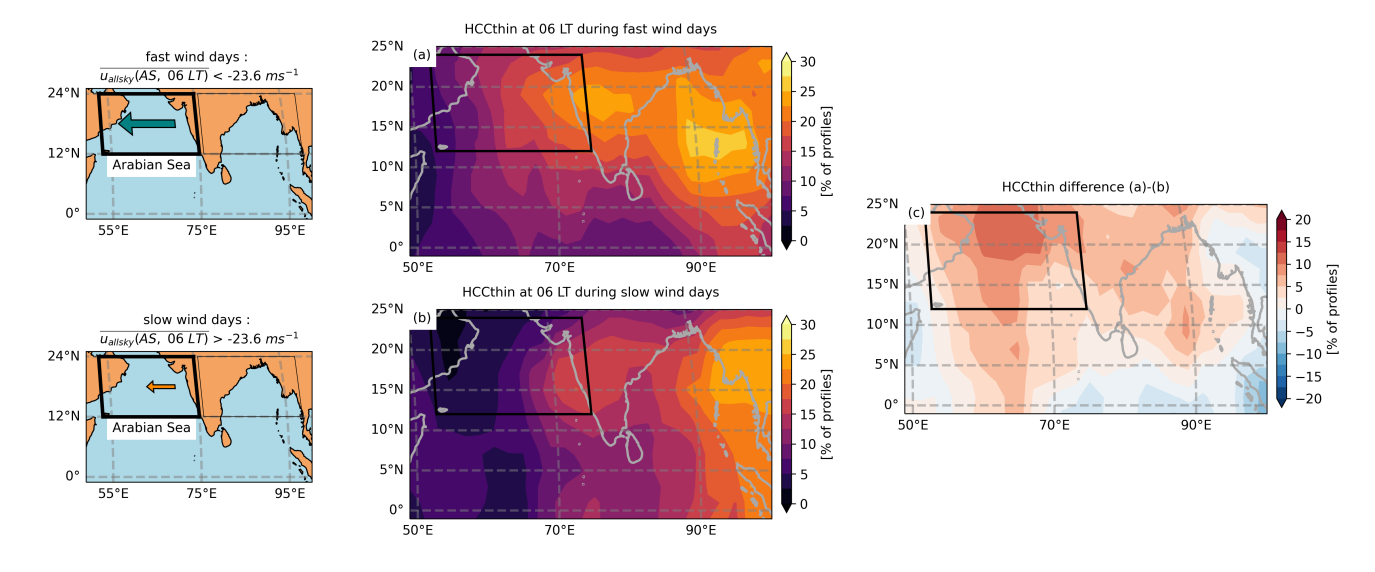


Figure 6. Average HCCthin at 06 LT over days where $\overline{u_{allsky}(AS, 06 LT)}$ is (a) faster and (b) slower than -23.6 ms⁻¹. (c) is the difference of (a)-(b).

225





Furthermore, Fig. 7a shows the PDFs of $u_{allsky}(AS, 06 LT)$ observed by Aeolus for each quartile of HCFthin(AS, 06 LT). Here, each occurrence of u_{allsky} and HCCthin corresponds to an average over the Arabian Sea for one given day at 06 LT and one given 480 m vertical level comprised between 14 and 17 km. The first quartile, median and third quartile of HCFthin(AS, 06 LT) are delimited respectively at 0.4 %, 2.6 % and 8 %. We note that all PDFs intersect between -15 and -20 ${\rm ms}^{-1}$. The first and second quartiles of $HCFthin(AS,~06~LT)~(\le 2.6~\%)$ are dominated by winds slower than -15 ms^{-1} , while the third and fourth quartiles of $HCFthin(AS, 06\ LT)$ (> 2.6 %) are dominated by winds faster than -20 ms^{-1} . $HCFthin(AS, 06\ LT) > 8\%$ are almost never observed over the Arabian Sea if $u_{allsky}(AS, 06\ LT)$ is slower than -10 ms⁻¹. The occurrences of observations of HCFthin(AS, 06 LT) > 8 % increase with wind speed and peak at -23 ms⁻¹, while the occurrences of having no thin clouds or $HCFthin(AS, 06\ LT) < 0.4\ \%$ peaks at -16 ms⁻¹. The sensitivity of HCFthinover the Arabian Sea to the wind is thus well established.

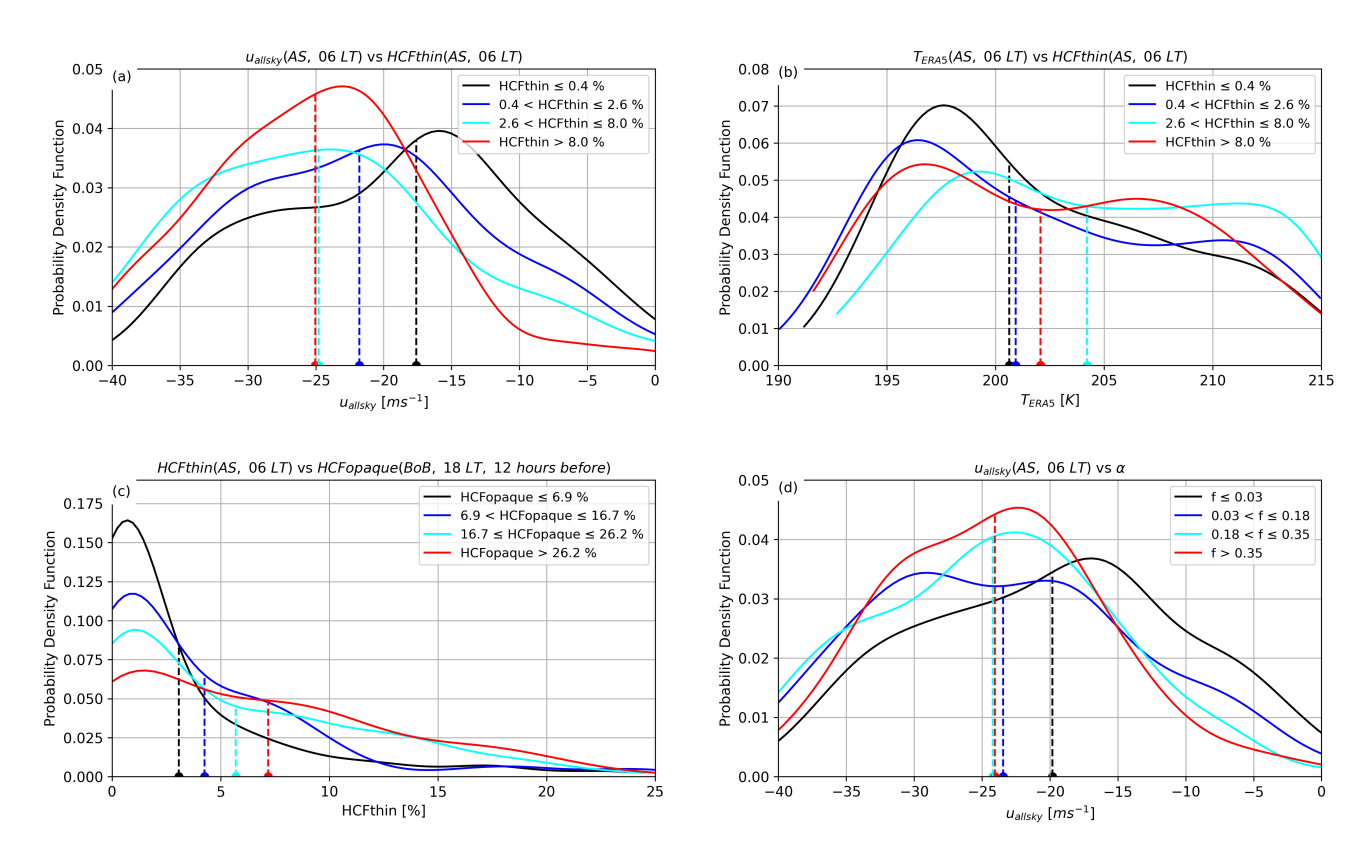


Figure 7. PDF of (a) $u_{allsky}(AS, 06 LT)$ and (b) the temperature averaged over the Arabian Sea at 06 LT (noted $T_{ERA5}(AS, 06 LT)$) for each quartile of HCFthin observed over the Arabian Sea at 06 LT, noted HCFthin(AS, 06 LT). (c) PDF of HCFthin(AS, 06 LT) for each quartile of HCF opaque observed over the Bay of Bengal (BoB) 12 hours before, at 18 LT, noted HCF opaque (BoB, 18 LT). (d) PDF of $u_{allsky}(AS, 06\ LT)$ for each quartile of the ratio α (see Eq. 1). Data are acquired each day during the SASM (June-October 2020), at each 480 m vertical level comprised between 14 and 17 km of altitude. The dotted lines represent the median values of each PDF.



230

235

240

245

250

255



4.2 Roles of temperature and opaque high cloud cover in thin high cloud cover variations

In this section, we consider two hypotheses: 1) negative temperature anomalies could occur when westward winds are strong over the Arabian Sea, and thus the presence of cirrus could be more explained by the thermodynamic conditions than by advection; 2) convective clouds could develop preferentially during strong westward winds over the Arabian Sea, and thus the higher occurrences of cirrus would be rather explained by a larger source of water vapour in the upper troposphere, than by advection.

4.2.1 Role of temperature

To test the first hypothesis, we consider the ERA5 air temperatures (Hersbach et al., 2020) co-located with Aeolus observations over the Arabian Sea from June to October 2020, during the SASM. We build the PDFs of ERA5 air temperatures (noted $T_{ERA5}(AS, 06\ LT)$) for each quartile of $HCFthin(AS, 06\ LT)$ (Fig. 7b). Each occurrence of $T_{ERA5}(AS, 06\ LT)$ here corresponds to an average over the Arabian Sea at 06 LT a given day and at a given 480 m vertical level comprised between 14 and 17 km. The temperatures corresponding to the PDFs maxima are 197.6 K, 196.3 K, 199.2 K and 196.7 K for the four quartiles of $HCFthin(AS, 06\ LT)$, sorted by increasing values of $HCFthin(AS, 06\ LT)$. The PDF of temperatures associated to the largest quartile of $HCFthin(AS, 06\ LT)$ (> 8.0 %) has a median value of 202.1 K, which is right between the median value of the third quartile of 204.2 K and the median values of the first and second quartiles (respectively 200.6 and 200.9 K). This shows that large values of $HCFthin(AS, 06\ LT)$ are not necessarily associated with low values of temperatures, and conversely low values of $HCFthin(AS, 06\ LT)$ are not associated with particularly high values of temperatures. Therefore we do not observe a significant dependency of $HCFthin(AS, 06\ LT)$ on temperatures experienced over the Arabian Sea between 14-17 km, and we can thus discard our first hypothesis.

4.2.2 Role of opaque high cloud cover

In order to test our second hypothesis, we build the composites of HCCopaque at 18 LT, depending on $u_{allsky}(AS, 06\ LT)$, the wind being observed 12 hours after the cloud cover is observed. Aeolus phasing has the fortunate property that on 3 days out of the 7-day cycle, the descending orbit of Aeolus over the Arabian Sea is located exactly 10.5° , or about $1150\ \mathrm{km}$ westward of the ascending orbit which overflew the Bay of Bengal or India 12 hours before blue(see for example the distance between the yellow orbit over the Arabian Sea on the 14 January 2020, and the light green orbit over India on the 13 January, Fig. 4). Consequently, an air parcel that is observed by Aeolus over the Bay of Bengal at 18 LT, and advected westward by the TEJ at about $30\ \mathrm{ms}^{-1}$ will be located around the Aeolus orbit track 12 hours later, over the Arabian Sea.

We note that 12 hours prior to fast wind days, HCCopaque is 29 % on average over India and the Bay of Bengal (Fig 8a), and maximum over North-East India at about 40 %; while 12 hours prior to slow wind days, it is on average 22 % and the maximum of HCCopaque of about 30 % is shifted southward (15°N, 78°E; fig 8b). The maximum of HCCopaque differences between fast and slow wind days is located over the North of India and reaches 20 % (fig. 8c). This change in the



265



location of the maximum of HCCopaque raises the question about the potential role of the location of deep convection on the zonal wind speed over the Arabian Sea, which will be discussed in Sect. 5.

These results also show that the fast wind days associated to higher HCCthin are also associated to larger HCCopaque over India and the Bay of Bengal. Thus we cannot exclude that the higher occurrences of thin clouds during these fast wind days are partly due to an increase in water vapour sources in the upper troposphere, transported upward by convection. However, over the Arabian Sea, the differences of HCCopaque between fast and slow wind days are weak, indicating that the additional sources of water vapour are not located where the cirrus are formed. We deduce that the thin clouds found over the Arabian Sea result from their advection over large distances.

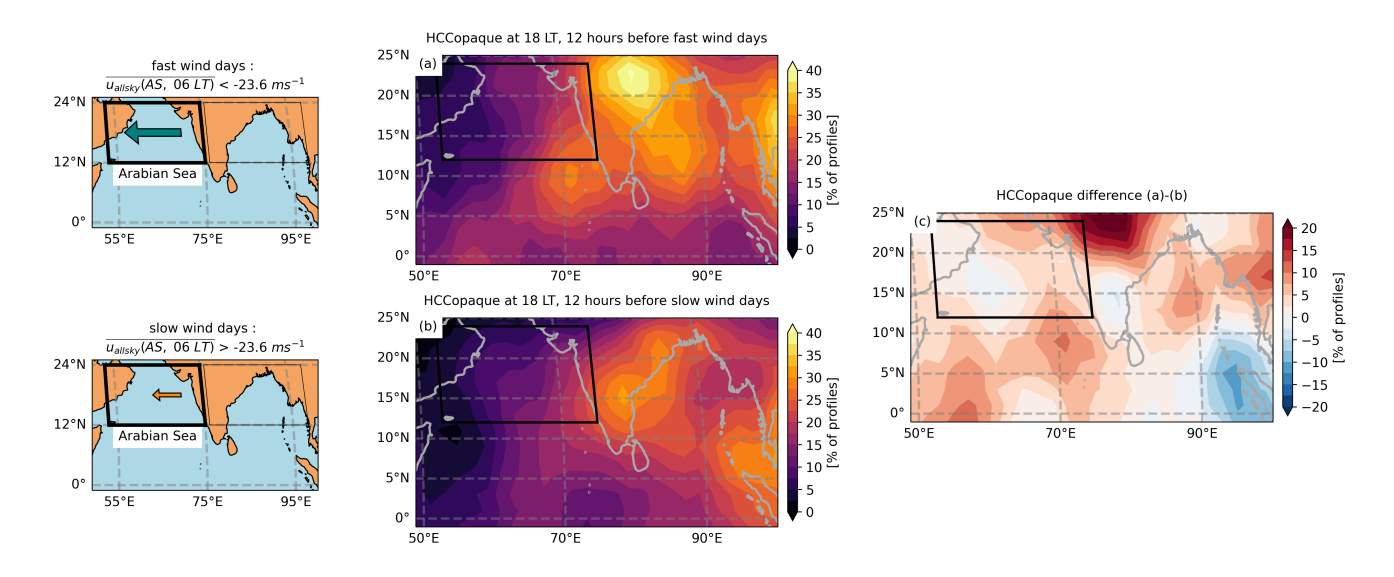


Figure 8. Average of high opaque high cloud cover HCCopaque at 18 LT over the days before $\overline{u_{allsky}(AS, 06 LT)}$ is (a) faster and (b) slower than -23.6 ms⁻¹. (c) is the difference of (a)-(b).

Figure 7c shows that indeed, larger HCFthin(AS,~06~LT) over the Arabian at 06 LT are likely to be associated to larger HCFopaque(BoB,~18~LT) observed over the Bay of Bengal (BoB) domain 12 hours before, at 18 LT, at the same altitude. For the four quartiles of HCFopaque(BoB,~18~LT) (delimited by 6.9 %, 16.7 %, 26.2%), the median values of HCFthin(AS,~06~LT) are 3 %, 4.5 %, 5.5 % and 7 % respectively. We conclude that higher occurrences of cirrus over the Arabian Sea may be explained by a combination of faster winds and larger sources of water vapour injected in the upper troposphere over India and the Bay of Bengal.

Finally, to disentangle the role of deep convection and upper tropospheric wind in the occurrence of thin clouds, we show in Fig. 7d four PDFs of $u_{allsky}(AS, 06 LT)$ for different values of α , with:



285



$$\alpha = \frac{HCFthin(AS, 06 LT)}{HCFopaque(BoB, 18LT) + HCFthin(AS, 06 LT)}$$
(1)

The parameter α is comprised between 0 and 1, and for any fixed value of $HCFopaque(BoB,\ 18\ LT)$, it increases when $HCFthin(AS,\ 06\ LT)$ increases. Furthermore, for any fixed value of $HCFthin(AS,\ 06\ LT)$, it increases when $HCFopaque(BoB,\ 18\ LT)$ decreases.

Figure 7d shows that at a given $HCFopaque(BoB,\ 18\ LT)$ observed over India or the Bay of Bengal at 18 LT, faster westward winds lead to a larger $HCFthin(AS,\ 06\ LT)$ (larger α) over the Arabian Sea 12 hours later, at 06 LT at the same altitude. This increase of $HCFthin(AS,\ 06\ LT)$ with respect to the $HCFopaque(BoB,\ 18\ LT)$ is particularly visible when the wind increases from -20 to -25 ms⁻¹, and then seems to form a plateau at -25 ms⁻¹, consistently with Fig. 7a, when the contribution of $HCFopaque(BoB,\ 18\ LT)$ is ignored. Therefore, these diagnostics show that both faster westward winds over the Arabian Sea, and larger $HCFopaque(BoB,\ 18\ LT)$ over the Bay of Bengal and North-East India contribute hand in hand to an increase of $HCFthin(AS,\ 06\ LT)$ over the Arabian Sea. A schematic is given in Fig. 9 to summarize our results.

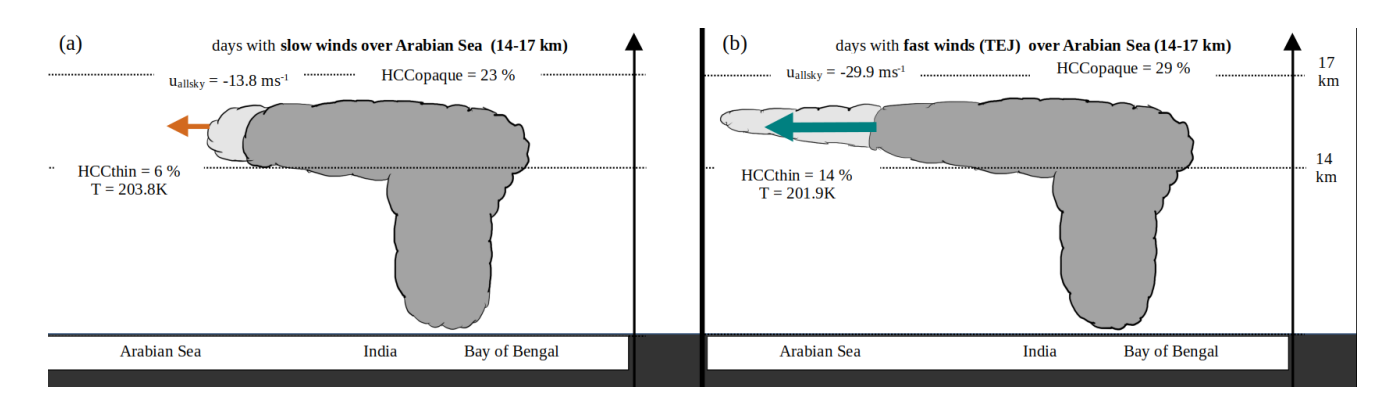


Figure 9. Schematic of the partition of thin and opaque high clouds over the Indian region on (a) slow days and (b) fast days.





5 Deep convection over the Bay of Bengal strengthens the Tropical Easterly Jet over the Arabian Sea

The goal of this section is to interpret the fluctuations of the TEJ speed over the Arabian Sea during SASM, by considering the respective roles of the variations of the large-scale North-South temperature gradient, and the changes in the convective patterns locations. In contrast to the studies of Ye et al. (2023) and Liu et al. (2024), our study does not focus on the specific location of the TEJ core and its interannual variability, but instead on TEJ speed fluctuations at a much shorter time scale (typically a few days).

295 5.1 Methodology

310

For this, we first compute the North-South temperature gradient over the domain of the Arabian Sea, depending on time and pressure. We use ERA5 air temperatures and pressures (Hersbach et al., 2020) and we evaluate this temperature difference at the longitude $\lambda(t)$ where the Aeolus measurement is performed at a given time:

$$\Delta T_{NS}(t,\lambda(t),p) = T_N(t,\lambda(t),p) - T_S(t,\lambda(t),p),\tag{2}$$

with $53^{\circ}E < \lambda(t) < 75^{\circ}E$. At a given time, longitude and pressure, T_N and T_S are the temperatures averaged between the latitudes $24^{\circ}N$ - $27^{\circ}N$, and $9^{\circ}N$ - $12^{\circ}N$ respectively, and thus correspond to the temperatures at the northern and southern borders of the Arabian Sea domain (more details are given in Fig. A1).

The zonal component of the thermal wind between 7 and 15 km, $\Delta u_g(t) = u_g(t, p_{z=15km}) - u_g(t, p_{z=7km})$, where u_g is the geostrophic wind, is then calculated following Eq. 3:

$$\Delta u_g(t) = \frac{R}{f} \int_{r_{cont}, r_{cont}}^{p_{z=15km}} \frac{\Delta T_{NS}(t, \lambda(t), p)}{\Delta y} d(\ln(p))$$
(3)

where R is the thermodynamic constant for dry air (287 JK⁻¹kg⁻¹), f is the Coriolis parameter estimated at the latitude $\theta_0 = 18^\circ N$ (the mean latitude of the Arabian Sea domain), $p_{z=7km}$ and $p_{z=15km}$ are the average pressures at the altitudes of 7 km and 15 km respectively. The length Δy is given by: $\Delta y = R_E \Delta \theta$, where R_E is the Earth radius and $\Delta \theta = 15$ deg is the latitude range over which the temperature difference is estimated.

We also estimate a longitudinal temperature difference ΔT_{EW} over the domain:

$$\Delta T_{EW}(t,p) = T_E(t,p) - T_W(t,p). \tag{4}$$

At a given time and pressure, the temperatures T_E and T_W are both averaged between the latitudes of $12^\circ N$ and $24^\circ N$, and between the longitudes $75^\circ E$ - $79^\circ E$ and $49^\circ E$ - $53^\circ E$ respectively. They thus correspond to the temperatures at the eastern and western borders of the Arabian Sea domain.





The meridional component of the thermal wind between 7 and 15 km $\Delta v_g(t) = v_g(t, p_{z=15km}) - v_g(t, p_{z=7km})$ is then calculated by the equation:

320
$$\Delta v_g(t) = -\frac{R}{f} \int_{p_{z=7km}}^{p_{z=15km}} \frac{\Delta T_{EW}(t,p)}{\Delta x} d(\ln(p))$$
 (5)

The length Δx is given by: $\Delta x = R_E cos(\theta_0) \Delta \lambda$, where $\Delta \lambda = 26$ deg is the longitude range over which the temperature difference is estimated.

We finally derive the projection of the thermal wind vector along the LOS of Aeolus (the direction in which the laser is pointing):

325
$$\Delta u_{thermal, ERA5}(t) = \sqrt{\Delta u_g(t)^2 + \Delta v_g(t)^2} \cdot \cos(\phi(t))$$
 (6)

where $\phi(t)$ is the angle formed between the thermal wind vector and the LOS of Aeolus. We note that because $\Delta v_g(t) \ll \Delta u_g(t)$, and because the horizontal projection is almost in the zonal direction, $\Delta u_{thermal, ERA5}(t)$ and $\Delta u_g(t)$ only differ by $1~{\rm ms}^{-1}$ at the highest.

We also compute the wind difference observed by Aeolus at the same altitudes as the thermal wind, for each descending orbit (06 LT) over the Arabian Sea following Eq. 7 (more details are given in Fig. A1).

$$\Delta u_{allsky} = u_{allsky}(z = 15km) - u_{allsky}(z = 7km) \tag{7}$$

5.2 Results

During the SASM, the median value of the difference $\Delta u_{allsky} - \Delta u_{thermal, ERA5}$ is equal to -2.1 ms⁻¹. This confirms that Δu_{allsky} can be interpreted at the first order by the thermal wind set by the North-South temperature gradient, or, in other words, that the TEJ is in thermal wind balance. We define $\Delta u'_{thermal, ERA5}$, the thermal wind corrected by the median of the difference $\Delta u_{allsky} - \Delta u_{thermal, ERA5}$:

$$\Delta u'_{thermal, ERA5}(t) = \Delta u_{thermal, ERA5}(t) - 2.1 \tag{8}$$





Figure 10 shows the time series of Δu_{allsky} and $\Delta u'_{thermal,\ ERA5}$ over the Arabian Sea at 06 LT between 1 June and 31 October 2020. As the SASM onsets in late May, both $\Delta u_{thermal,\ ERA5}$ and Δu_{allsky} decrease at the same rate to reach values of about -35 ms⁻¹ in early August, coinciding with the date of the maximum intensity of the TEJ over the Arabian Sea, before increasing again at similar rates.

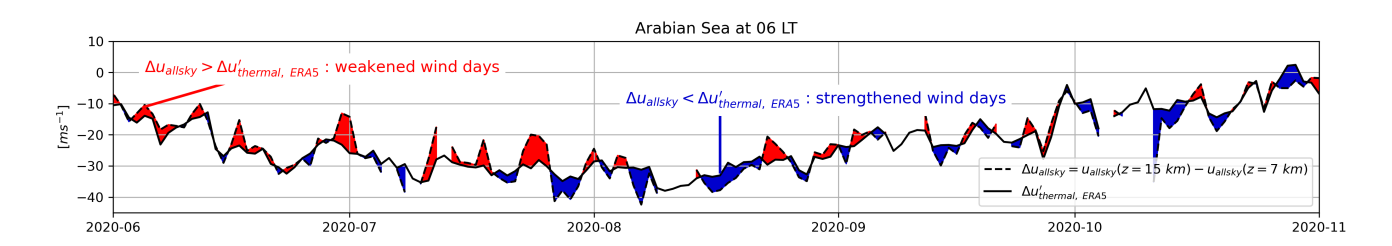


Figure 10. (a) Time series of Δu_{allsky} (dashed black line) and $\Delta u'_{thermal,\ ERA5}$ (solid black line) over the Arabian Sea at 06 LT. Red shading means that $\Delta u_{allsky} > \Delta u'_{thermal,\ ERA5}$ and blue shading means that $\Delta u_{allsky} < \Delta u'_{thermal,\ ERA5}$.

From June to October 2020, there are exactly 69 days where $\Delta u_{allsky} < \Delta u'_{thermal,\ ERA5}$, 69 days where $\Delta u_{allsky} > \Delta u'_{thermal,\ ERA5}$, and 7 days without Aeolus observations (Fig. 10). The fluctuations of Δu_{allsky} around $\Delta u'_{thermal,\ ERA5}$ can be explained by the effects of deep convection patterns on Δu_{allsky} , that act as perturbations on the first order approximation of Δu_{allsky} . We expect these perturbations of Δu_{allsky} to affect mainly u_{allsky} around 15 km of altitude (rather than u_{allsky} around 7 km of altitude), because the wind divergence and vorticity associated to deep convection are strongest at the top of convective towers (Diongue et al., 2002). We define u_{conv} as the difference:

$$u_{conv}(t) = \Delta u_{allsky}(t) - \Delta u'_{thermal ERA5}(t) \tag{9}$$

We can thus interpret u_{conv} as the convective perturbation of $u_{allsky}(AS,~06~LT)$. In Fig. 11, we consider two ensembles of days. The days where $\Delta u_{allsky} < \Delta u'_{thermal,~ERA5}$ at 06 LT over the Arabian Sea are referred as "strengthened" wind days with respect to the thermal wind, and shaded in blue in Fig. 11. Oppositely, the days where $\Delta u_{allsky} > \Delta u'_{thermal,~ERA5}$ at 06 LT over the Arabian Sea are referred as "weakened" wind days with respect to the thermal wind, and shaded in red in Fig. 11. The fluctuations of Δu_{allsky} around $\Delta u'_{thermal,~ERA5}$ usually have a short time scale (of one day) but they can be as long as two weeks (in mid August 2020 for example). For each of these ensembles, we build the composite maps of HCCopaque (between 14 and 17 km) observed at 18 LT the day before the winds are observed.





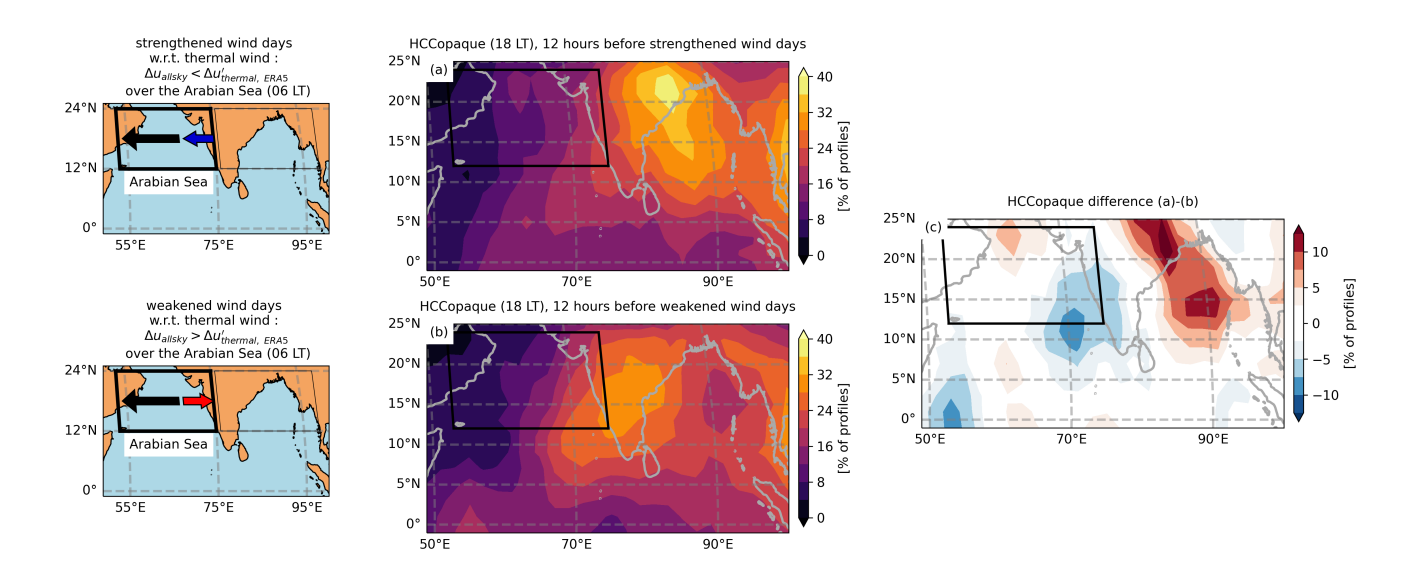


Figure 11. (a) Composite maps of the opaque high cloud cover HCCopaque between 14 and 17 km of altitude at 18 LT the day before strengthened wind days ($\Delta u_{allsky} < \Delta u'_{thermal,\ ERA5}$ over the Arabian Sea at 06 LT). (b) same but for weakened wind days ($\Delta u_{allsky} > \Delta u'_{thermal,\ ERA5}$ over the Arabian Sea at 06 LT). The black arrow represents the thermal wind background, blue and red arrows respectively represent the westward and eastward Δu_{allsky} perturbation over the Arabian Sea. (c) is the difference (a)-(b).





Twelve hours before the strengthened wind days, we observe a maximum of HCCopaque over the North-East of India (of about 40 %) and another maximum over the Bay of Bengal (of 29 %) (Fig. 11a). Over the South-East of the Arabian Sea, HCCopaque is about 20 % and on average 11 % over the entire Arabian Sea. In contrast, 12 hours before the weakened wind days, the maximum of HCCopaque is found over the centre and the West of India, while the HCCopaque only reaches 23 % over the Bay of Bengal, about 30 % over the South-East of the Arabian Sea and 14 % on average over the entire Arabian Sea (Fig. 11b). We thus observe that HCCopaque at 18 LT over the Bay of Bengal is in phase opposition with HCCopaque over the South-East of the Arabian Sea. The amplitude of the changes of HCCopaque between strengthened and weakened wind days is about 3 % over the Arabian Sea and 6 % over the Bay of Bengal (Fig. 11c). Liu et al. (2024) revealed the existence of a similar deep convection dipole at the same location, which exhibits a large interannual variability in July.

The deep convection dipole depicted in Fig. 11 is thus partly responsible for fluctuations of the wind downstream, particularly over the Eastern part of the Arabian Sea. This is understandable having in mind that Deep Convective Systems (DCS) are associated at their top with a divergent outflow and a negative vorticity, which induce an eastward wind perturbation in the North-East and a westward wind perturbation in the South-West (Diongue et al., 2002). Lemburg et al. (2019) described a similar phenomenon occurring over the Sahel region, which induces a westward (negative) perturbation of the TEJ of about -1.5 ms^{-1} at the South-West of the DCS at around 200 hPa, and an eastward (positive) perturbation of the TEJ of about 1 ms^{-1} at the North-East of the DCS at the same pressure level. Lemburg et al. (2019) further showed that the wind perturbation was felt up to 2 days after the growth of the DCS.

375

380

370

360

365

During strengthened wind days, 12 hours after HCCopaque is maximum over the Bay of Bengal and North-East India, its divergent convective outflow, deflected in a clockwise motion by the Coriolis force, strengthens the westward wind at the South-West of the Bay of Bengal (Fig. 12c). This strengthening of the wind (a westward, thus negative wind perturbation u_{conv}) is favoured by the weakening of the divergent convective outflow over the South-East Arabian Sea. Inversely, 12 hours after HCCopaque is maximum over the South-East Arabian Sea, the divergent outflow at the North-East of this convection maximum induces an eastward, thus positive u_{conv} perturbation over India, that is less counter acted by the weaker diverging outflow over the Bay of Bengal and North-East India (Fig. 12b).





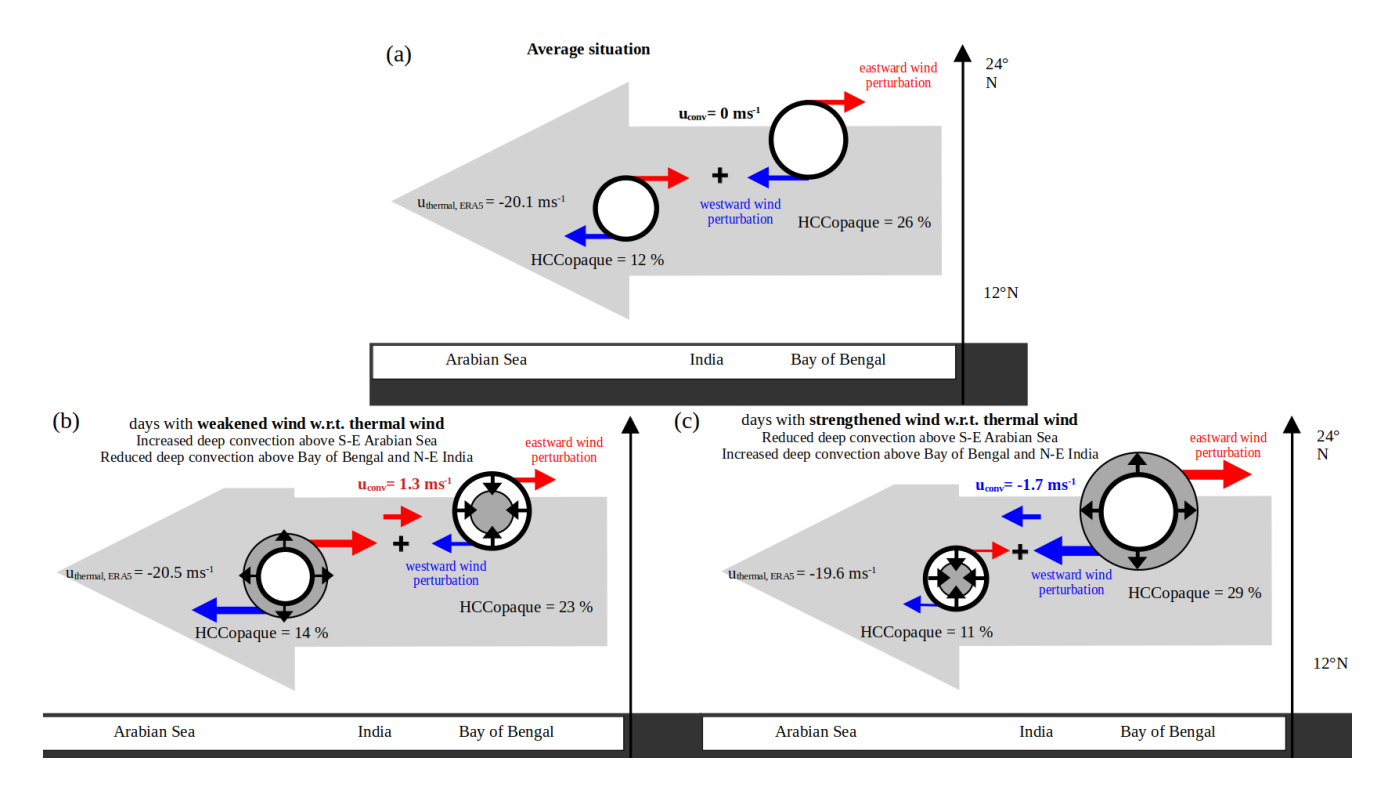


Figure 12. Schematic of the mechanisms inducing a wind anomaly over the Arabian Sea at 06 LT. (a) Describes the average situation. (b) Describes the high cloud cover and wind values on days where $\Delta u_{allsky} > \Delta u'_{thermal,\ ERA5}$ over the Arabian Sea (weakened winds), and (c), the high cloud cover and wind values on days where $\Delta u_{allsky} < \Delta u'_{thermal,\ ERA5}$ over the Arabian Sea (strengthened winds). Thick black circles with a white shading represent the average high cloud covers of the dipole. Thin black circles with a dark brown shading represent the actual high cloud cover, to compare with the average value. Large gray arrows represent the wind induced by the temperature gradient.





The vorticity difference between strengthened and weakened wind days $\Delta \xi = \xi^{strengthened} - \xi^{weakened}$ can be calculated from the wind difference $u_{allsky}^{strengthened} - u_{allsky}^{weakened}$ displayed in Fig. 13c, following Eq. 10:

385
$$\Delta \xi = -\frac{\partial}{\partial y} \left(u_{allsky}^{strengthened} - u_{allsky}^{weakened} \right).$$
 (10)

We estimate the vorticity difference $\Delta \xi_{P_N P_S}$ between the points P_N and P_S , respectively located in the North and South of the HCCopaque pattern over the Arabian Sea (Fig. 13c) following Eq. 11:

$$\Delta \xi_{P_N P_S} = -\frac{u_{allsky}^{strengthened}(P_N) - u_{allsky}^{strengthened}(P_S) - u_{allsky}^{weakened}(P_N) + u_{allsky}^{weakened}(P_S)}{y(P_N) - y(P_S)}$$
(11)

where $y(P_N)-y(P_S)$ is the distance between the points P_N and P_S . Similarly, we estimate the vorticity difference $\Delta \xi_{Q_NQ_S}$ 390 between the points Q_N and Q_S , respectively located in the North and South of the HCCopaque pattern over the Bay of Bengal (Fig. 13c). As expected, at 06 LT, we find a positive vorticity around the HCCopaque pattern over the South-East of the Arabian Sea ($\Delta \xi_{P_NP_S} = 1.04 \times 10^{-6} \text{ s}^{-1}$), and a negative vorticity around the HCCopaque pattern over the Bay of Bengal ($\Delta \xi_{Q_NQ_S} = -1.69 \times 10^{-6} \text{ s}^{-1}$).

As the wind perturbations created by deep convection propagate during the night with the mean flow (Lemburg et al., 2019), we observe that on average over the whole Arabian Sea, u_{conv} reaches -1,7 ms⁻¹ during strengthened wind days at 06 LT. On the other hand, over weakened wind days, u_{conv} is equal to 1.3 ms⁻¹ over the Arabian Sea at 06 LT, so the total amplitude variation of the wind induced by the deep convective activity is about -3 ms⁻¹ on average over the Arabian Sea, and reaches up to -5 ms⁻¹ in its center (Fig. 13c). Note that when HCCopaque is maximum over the Bay of Bengal and North-East India, there is also a positive wind perturbation of up to 3 ms⁻¹, at 25°N, which is favored by the larger Coriolis parameter at this latitude (Fig. 13c).





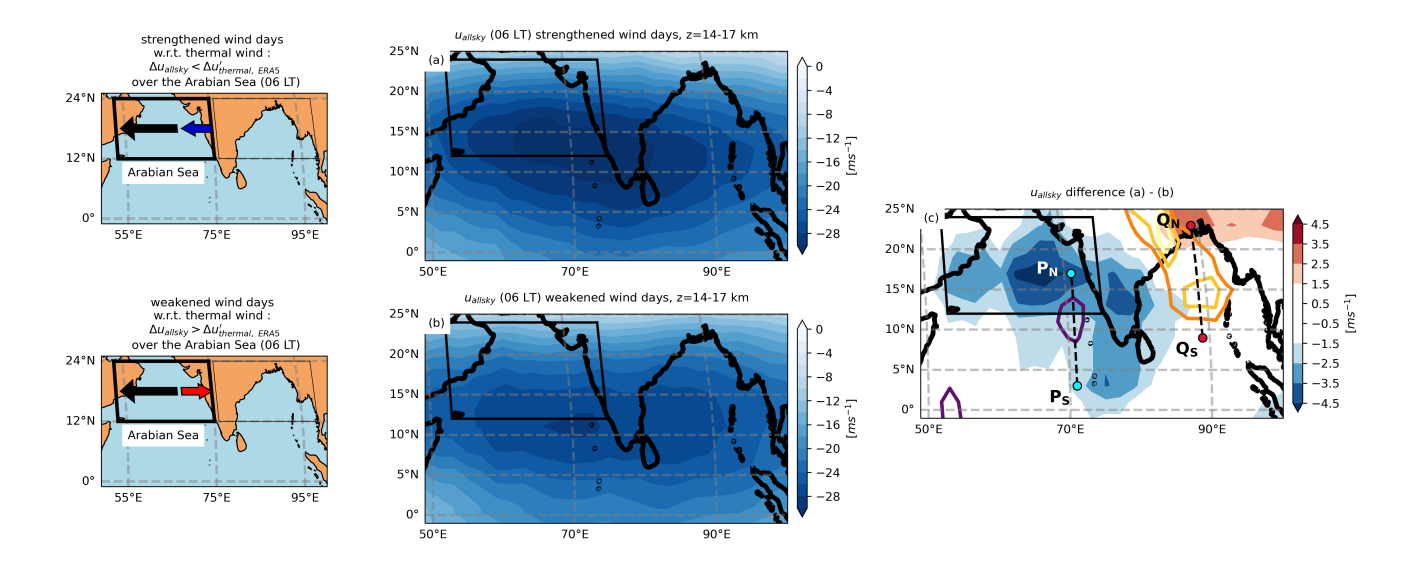


Figure 13. Same as Fig. 11, but for $u_{allsky}(AS, 06\ LT)$ averaged between 14 and 17 km of altitude instead of $HCCopaque(BoB, 18\ LT)$. (c) the contours represent the difference of $HCCopaque(BoB, 18\ LT)$ between strengthened and weakened wind days as depicted on 11c.





6 Conclusion

We evaluated the relationships between thin clouds, opaque clouds, and the wind above the Indian region during the South-Asian summer monsoon 2020 with Aeolus observations. We found that thin cloud fractions over the Arabian Sea between 14 and 17 km of altitude were sensitive to the wind speed at the same altitude. We noted that the thin high cloud cover spatially averaged over the Arabian Sea at 06 LT increases from 6 % to 14 % when the westward wind speed over the Arabian Sea doubles (from 13.8 ms⁻¹ to 29.9 ms⁻¹). Thin high cloud fraction profiles larger than 8 % are almost never observed over the Arabian Sea for westward winds slower than 10 ms⁻¹, but are observed more frequently when the westward wind speed increases. We do not observe a significant dependency of thin high cloud fractions on temperatures, therefore the thermodynamic conditions are not the limiting factor controlling the formation of cirrus over the Arabian Sea during SASM. In contrast, larger thin high cloud fractions over the Arabian Sea at 06 LT are associated to larger opaque high cloud fractions over the Bay of Bengal 12 hours before. We conclude that the thin clouds found over the Arabian Sea result from their detrainment and advection over large distances, and that they are more frequent when westward winds are faster and when larger sources of water vapour are injected in the upper troposphere over India and the Bay of Bengal.

415

420

425

430

435

405

410

By computing the thermal wind between 7 and 15 km over the Arabian Sea and by comparing it to the wind speed difference observed with Aeolus between these two altitudes, we showed that the TEJ variations during SASM can be explained to a large extent by the variations in the North-South temperature gradient calculated over the Arabian Sea. However, some days showed a strengthened TEJ compared to what would be expected from the temperatures, and these days were associated to the presence of more deep convection in the North of the Bay of Bengal and less deep convection over the South-East Arabian Sea 12 hours before. Conversely, the days that showed a weakened TEJ compared to what what would be expected from the temperatures, were associated to more deep convection over the South-East of the Arabian Sea and less deep convection over the North of the Bay of Bengal 12 hours before. We then concluded that deep convection anomalies, via their associated circulations, modulate the TEJ over the Arabian Sea, following a process similar to the one described by Lemburg et al. (2019) over the Sahel. The TEJ modulation lags deep convection anomalies by 12 hours, suggesting that deep convection anomalies are more likely to drive changes in the regional TEJ than vice versa. Additionally, the same dipole of deep convection was found to explain the interannual longitudinal variability of the TEJ core (Liu et al., 2024) in July. We then show that the dipole modulates the TEJ wind speed over the Arabian Sea on shorter time scales of one, up to a few days.

inten pathy from

The TEJ shows a decreasing trend in the reanalyses during the period 1958–1998 (Rao et al., 2004) and the central TEJ intensity is expected to weaken by 18 % over the Indian Ocean by the end of the 21^{st} century under the shared socioeconomic pathway 5–8.5, according to CMIP simulations (Huang et al., 2020). As the cirrus cover over the Arabian Sea mostly results from the advection of water vapour caused by a strong TEJ, one can thus expect a decrease of the cirrus cloud cover in this region in the future. Assuming that the shape of the westward wind distribution over the Arabian Sea is conserved, but that its mean is reduced by 18 %, the number of days with a westward wind slower than 10 ms⁻¹ would increase from 17 (present) to



445



28 (end of century). If all other parameters (temperature, deep convection intensity and patterns) remained constant, this would then increase similarly the number of cirrus-free days over the Arabian Sea. The hypothesis of other constant parameters seem nevertheless very unrealistic. Indeed, Rao et al. (2004) noticed over 40 years a decrease in the number of tropical cyclones over the Bay of Bengal, and by the end of our century, the CMIP simulations project a suppressed rainfall over the tropical eastern Indian Ocean (Huang et al., 2020). This trend in convection could thus amplify the decrease of the cirrus cloud cover over the Arabian Sea, because the deep convective sources of water vapour would be diminished. According to Huang et al. (2020) the deep convective trend over the eastern Indian Ocean might explain 18 % of the weakening of the TEJ through generating an upper-level convergence and favoring divergent westerly wind over the tropical Indian Ocean. This relationship between convection and the TEJ intensity, valuable at interannual time scales, is thus similar to the one suggested by our results, at a synoptic scale.

In the future, we plan to investigate further the relationships between the TEJ, deep convection and cirrus cloud cover over the Indian Ocean in a Global Circulation Model, in the current climate and in a warming climate, with different socio-economic scenarios.





450 . ALADIN/Aeolus orbit gridded data presented in this paper are available via AERIS (https://dx.doi.org/10.25326/746). They are built from Aeolus Level 1A and Level 2B observations that can be accessed via the ESA Aeolus Online Dissemination System (https://aeolus-ds.eo.esa.int/oads/access/). ERA5 reanalyses (Hersbach et al., 2020) were accessible via Mesocentre ESPRI/IPSL.

Appendix A: Complements relative to composite maps and wind observations

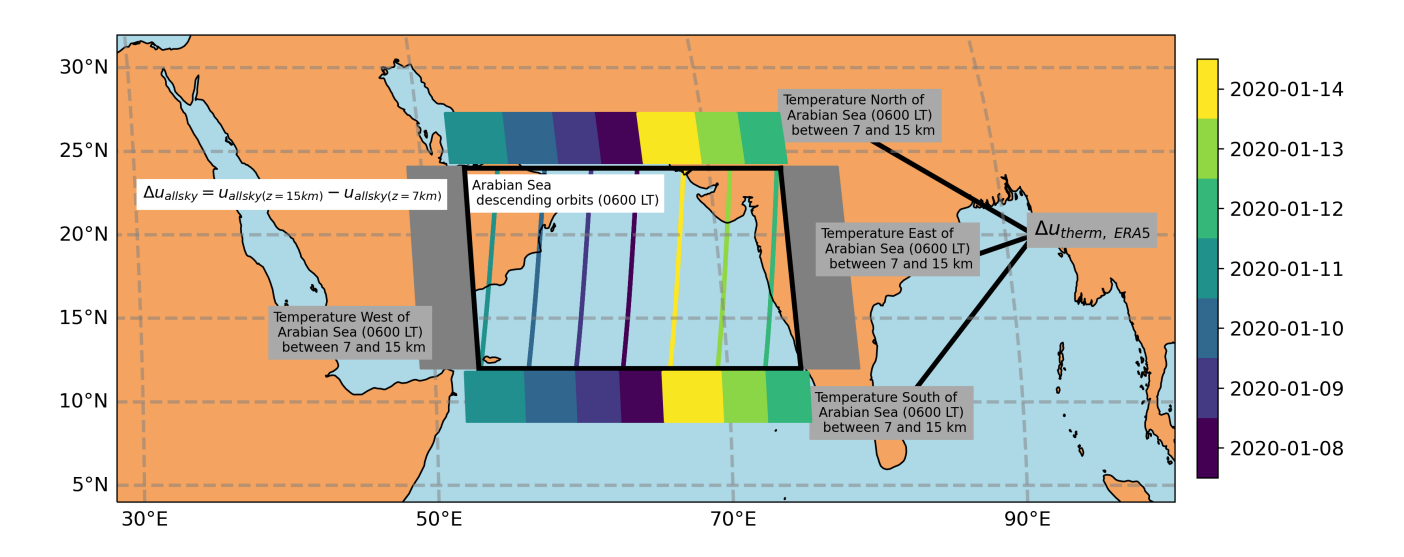


Figure A1. Schematic of (a) the calculations of Δu_{allsky} , the wind speed difference observed between 15 and 7 km of altitude by Aeolus over the Arabian Sea at 06 LT and (b) the derivation of the $\Delta u_{therm,ERA5}$, the thermal wind between 15 and 7 km of altitude, also over the Arabian Sea at 06 LT.





	. ZT, MB, and HC drafted the article. The Aeolus dataset development was performed by ZT and AGF. The data analysis was performed by
455	ZT and MB. All authors were involved in the writing and investigation.

- . The authors declare that they have no conflict of interest.
- . The authors thank Mesocentre ESPRI/IPSL for the computation resources. We also thank ESA dissemination team for the access to Aeolus data and AERIS for the storage of the dataset.





References

- 460 Ackerman, T. P., Liou, K.-N., Valero, F. P., and Pfister, L.: Heating rates in tropical anvils, Journal of Atmospheric Sciences, 45, 1606–1623, https://doi.org/10.1175/1520-0469(1988)045<1606:HRITA>2.0.CO;2, 1988.
 - Ali, S., Mehta, S. K., Ananthavel, A., and Reddy, T. V. R.: Temporal and vertical distributions of the occurrence of cirrus clouds over a coastal station in the Indian monsoon region, Atmospheric Chemistry and Physics, 22, 8321–8342, https://doi.org/10.5194/acp-22-8321-2022, 2022.
- Betts, A.: Non-precipitating cumulus convection and its parameterization, Quarterly Journal of the Royal Meteorological Society, 99, 178–196, https://doi.org/10.1002/qj.49709941915, 1973.
 - Chen, S. S. and Houze Jr, R. A.: Diurnal variation and life-cycle of deep convective systems over the tropical Pacific warm pool, Quarterly Journal of the Royal Meteorological Society, 123, 357–388, https://doi.org/10.1002/qj.49712353806, 1997.
- Chen, T.-C.: On the kinetic energy budget of the summer-mean flow at 200 mb in the tropics, Tellus, 34, 55–62, https://doi.org/10.1111/j.2153-3490.1982.tb01792.x, 1982.
 - Chen, T.-C. and van Loon, H.: Interannual variation of the tropical easterly jet, Monthly Weather Review, 115, 1739–1759, https://doi.org/10.1175/1520-0493(1987)115<1739:IVOTTE>2.0.CO;2, 1987.
 - Chepfer, H., Brogniez, H., and Noel, V.: Diurnal variations of cloud and relative humidity profiles across the tropics, Scientific reports, 9, 16 045, https://doi.org/10.1038/s41598-019-52437-6, 2019.
- 475 Corcos, M., Hertzog, A., Plougonven, R., and Podglajen, A.: A simple model to assess the impact of gravity waves on ice-crystal populations in the tropical tropopause layer, Atmospheric Chemistry and Physics, 23, 6923–6939, https://doi.org/=10.5194/acp-23-6923-2023, 2023.
 - Das, S. K., Chiang, C.-W., and Nee, J.-B.: Influence of tropical easterly jet on upper tropical cirrus: an observational study from CALIPSO, Aura-MLS, and NCEP/NCAR data, Journal of Geophysical Research: Atmospheres, 116, https://doi.org/=10.1029/2011JD015923, 2011.
- Diongue, A., Lafore, J.-P., Redelsperger, J.-L., and Roca, R.: Numerical study of a Sahelian synoptic weather system:

 Initiation and mature stages of convection and its interactions with the large-scale dynamics, Quarterly Journal of the Royal Meteorological Society: A journal of the atmospheric sciences, applied meteorology and physical oceanography, 128, 1899–1927, https://doi.org/=10.1256/003590002320603467, 2002.
 - Donovan, D. P., van Zadelhoff, G.-J., and Wang, P.: The EarthCARE lidar cloud and aerosol profile processor (a-PRO): The a-AER, a-EBD, a-TC, and a-ICE products, Atmospheric Measurement Techniques, 17, 5301–5340, https://doi.org/10.5194/amt-17-5301-2024, 2024.
- Feofilov, A. G. and Stubenrauch, C. J.: Diurnal variation of high-level clouds from the synergy of AIRS and IASI space-borne infrared sounders, Atmospheric Chemistry and Physics, 19, 13 957–13 972, https://doi.org/10.5194/acp-19-13957-2019, 2019.
 - Feofilov, A. G., Chepfer, H., Noël, V., Guzman, R., Gindre, C., Ma, P.-L., and Chiriaco, M.: Comparison of scattering ratio profiles retrieved from ALADIN/Aeolus and CALIOP/CALIPSO observations and preliminary estimates of cloud fraction profiles, Atmospheric Measurement Techniques, 15, 1055–1074, https://doi.org/10.5194/amt-15-1055-2022, 2022.
- 490 Gasparini, B., Rasch, P. J., Hartmann, D. L., Wall, C. J., and Dütsch, M.: A Lagrangian perspective on tropical anvil cloud lifecycle in present and future climate, Journal of Geophysical Research: Atmospheres, 126, e2020JD033487, https://doi.org/10.1029/2020JD033487, 2021.
 - Hartmann, D. L. and Berry, S. E.: The balanced radiative effect of tropical anvil clouds, Journal of Geophysical Research: Atmospheres, 122, 5003–5020, https://doi.org/10.1002/2017JD026460, 2017.
- Hersbach, H., Bell, B., Berrisford, P., Hirahara, S., Horányi, A., Muñoz-Sabater, J., Nicolas, J., Peubey, C., Radu, R., Schepers, D., et al.: The ERA5 global reanalysis, Quarterly journal of the royal meteorological society, 146, 1999–2049, https://doi.org/10.1002/qj.3803, 2020.



515

530



- Höjgård-Olsen, E., Chepfer, H., and Brogniez, H.: Satellite observed sensitivity of tropical clouds and moisture to sea surface temperature on various time and space scales: 1. Focus on high level cloud situations over ocean, Journal of Geophysical Research: Atmospheres, 127, e2021JD035 438, https://doi.org/10.1029/2021JD035438, 2022.
- Huang, S., Wang, B., and Wen, Z.: Dramatic Weakening of the Tropical Easterly Jet Projected by CMIP6 Models, Journal of Climate, 33, 8439–8455, https://doi.org/10.1175/JCLI-D-19-1002.1, 2020.
 - Iqbal, W., Syed, F., Sajjad, H., Nikulin, G., Kjellström, E., and Hannachi, A.: Mean climate and representation of jet streams in the CORDEX South Asia simulations by the regional climate model RCA4, Theoretical and Applied Climatology, 129, 1–19, https://doi.org/10.1007/s00704-016-1755-4, 2017.
- Jensen, E., Ueyama, R., Pfister, L., and Atlas, R.: The impacts of gravity waves and wind shear on the lifecycle of cirrus clouds in the tropical tropopause layer, Journal of Geophysical Research: Atmospheres, 130, e2024JD042308, https://doi.org/10.1029/2024JD042308, 2025.
 - Koteswaram, P.: The easterly jet stream in the tropics, Tellus, 10, 43-57, https://doi.org/10.3402/tellusa.v10i1.9220, 1958.
 - Kripalani, R., Ha, K.-J., Ho, C.-H., Oh, J.-H., Preethi, B., Mujumdar, M., and Prabhu, A.: Erratic Asian summer monsoon 2020: COVID-19 lockdown initiatives possible cause for these episodes?, Climate Dynamics, 59, 1339–1352, https://doi.org/10.1007/s00382-021-06042-x, 2022.
- Krishnamurthy, V. and Shukla, J.: Intraseasonal and interannual variability of rainfall over India, Journal of climate, 13, 4366–4377, https://doi.org/10.1175/1520-0442(2000)013<0001:IAIVOR>2.0.CO;2, 2000.
 - Krishnamurti, T., Daggupaty, S., Fein, J., Kanamitsu, M., and Lee, J. D.: Tibetan high and upper tropospheric tropical circulations during northern summer, Bulletin of the American Meteorological Society, 54, 1234–1250, https://doi.org/10.1175/1520-0477-54.12.1234, 1973.
 - Lemburg, A., Bader, J., and Claussen, M.: Sahel rainfall–tropical easterly jet relationship on synoptic to intraseasonal time scales, Monthly Weather Review, 147, 1733–1752, https://doi.org/10.1175/MWR-D-18-0254.1, 2019.
 - Liu, S., Huang, S., Tan, Y., Wen, Z., Chen, X., and Guo, Y.: Characteristics and mechanisms of the interannual variability of the Northwest–Southeast shift of the tropical easterly Jet's core in July, Journal of Climate, 37, 3219–3235, https://doi.org/10.1175/JCLI-D-23-0291.1, 2024.
- Luo, Z. and Rossow, W. B.: Characterizing tropical cirrus life cycle, evolution, and interaction with upper-tropospheric water vapor using

 Lagrangian trajectory analysis of satellite observations, Journal of climate, 17, 4541–4563, https://doi.org/10.1175/3222.1, 2004.
 - Mapes, B. E. and Houze Jr, R. A.: Cloud clusters and superclusters over the oceanic warm pool, Monthly Weather Review, 121, 1398–1416, https://doi.org/10.1175/1520-0493(1993)121<1398:CCASOT>2.0.CO;2, 1993.
 - Massie, S., Gettelman, A., Randel, W., and Baumgardner, D.: Distribution of tropical cirrus in relation to convection, Journal of Geophysical Research: Atmospheres, 107, AAC–19, https://doi.org/10.1029/2001JD001293, 2002.
- McKim, B., Bony, S., and Dufresne, J.-L.: Weak anvil cloud area feedback suggested by physical and observational constraints, Nature Geoscience, 17, 392–397, https://doi.org/10.1038/s41561-024-01414-4, 2024.
 - Mehta, S. K.: Observational evidence of the relationship between the tropical tropopause and tropical easterly jet streams over the Indian monsoon region, Atmospheric Science Letters, 25, https://doi.org/10.1002/asl.1230, 2024.
 - Mohan, T. and Rao, T.: Differences in the mean wind and its diurnal variation between wet and dry spells of the monsoon over southeast India, Journal of Geophysical Research: Atmospheres, 121, 6993–7006, https://doi.org/10.1002/2015JD024704, 2016.
 - Nicholson, S. E.: On the factors modulating the intensity of the tropical rainbelt over West Africa, International Journal of Climatology: A Journal of the Royal Meteorological Society, 29, 673–689, https://doi.org/10.1002/joc.1702, 2009.



535

540

555



- Noel, V., Chepfer, H., Chiriaco, M., and Yorks, J.: The diurnal cycle of cloud profiles over land and ocean between 51 S and 51 N, seen by the CATS spaceborne lidar from the International Space Station, Atmospheric Chemistry and Physics, 18, 9457–9473, https://doi.org/10.5194/acp-18-9457-2018, 2018.
 - Pattanaik, D. and Satyan, V.: Fluctuations of tropical easterly jet during contrasting monsoons over India: A GCM study, Meteorology and Atmospheric Physics, 75, 51–60, https://doi.org/10.1007/s007030070015, 2000.
 - Rao, B. S., Rao, D. B., and Rao, V. B.: Decreasing trend in the strength of Tropical Easterly Jet during the Asian summer monsoon season and the number of tropical cyclonic systems over Bay of Bengal, Geophysical Research Letters, 31, https://doi.org/10.1029/2004GL019817, 2004.
 - Reitebuch, O.: The spaceborne wind lidar mission ADM-Aeolus, in: Atmospheric physics: Background–methods–trends, pp. 815–827, Springer, https://doi.org/10.1007/978-3-642-3, 2012.
- Sathiyamoorthy, V., Pal, P., and Joshi, P.: Intraseasonal variability of the tropical easterly jet, Meteorology and Atmospheric Physics, 96, 305–316, 2007.
- 545 Shenoi, S., Nasnodkar, N., Rajesh, G., Jossia Joseph, K., Suresh, I., and Almeida, A.: On the diurnal ranges of Sea Surface Temperature (SST) in the north Indian Ocean, Journal of Earth System Science, 118, 483–496, https://doi.org/10.1007/s12040-009-0038-1, 2009.
 - Stoffelen, A., Pailleux, J., Källén, E., Vaughan, J. M., Isaksen, L., Flamant, P., Wergen, W., Andersson, E., Schyberg, H., Culoma, A., et al.: The atmospheric dynamics mission for global wind field measurement, Bulletin of the American Meteorological Society, 86, 73–88, https://doi.org/10.1175/BAMS-86-1-73, 2005.
- Stubenrauch, C. J., Bonazzola, M., Protopapadaki, S. E., and Musat, I.: New cloud system metrics to assess bulk ice cloud schemes in a GCM, Journal of Advances in Modeling Earth Systems, 11, 3212–3234, https://doi.org/10.1029/2019MS001642, 2019.
 - Titus, Z., Bonazzola, M., Chepfer, H., Feofilov, A. G., Roussel, M.-L., Witschas, B., and Bastin, S.: Wind-cloud interactions observed with Aeolus spaceborne Doppler Wind Lidar, Atmospheric Chemistry and Physics, https://doi.org/10.5194/egusphere-2025-2065, 2025.
 - Yang, P., Hong, G., Dessler, A. E., Ou, S. S., Liou, K.-N., Minnis, P., and Harshvardhan: Contrails and induced cirrus: Optics and radiation, Bulletin of the American Meteorological Society, 91, 473–478, https://doi.org/10.1175/2009BAMS2837.1, 2010.
 - Ye, J., Guo, Y., Wen, Z., Zhao, P., and Huang, S.: Longitudinal oscillation mode of the tropical easterly jet in June: role of precipitation anomalies in Asian monsoon region, Climate Dynamics, 60, 1543–1558, https://doi.org/10.1007/s00382-022-06391-1, 2023.
 - Zuidema, P.: Convective clouds over the Bay of Bengal, Monthly Weather Review, 131, 780–798, https://doi.org/10.1175/1520-0493(2003)131<0780:ccotbo>2.0.co;2, 2003.